

<https://doi.org/10.1038/s40494-025-01583-4>

How to approach long-term monitoring of chemical dynamics in oil paintings?



Jorien R. Duivenvoorden^{1,2}✉, Piotr Targowski³, Marcin Sylwestrzak³, Magdalena Iwanicka⁴, Jana Striova⁵, Diego Quintero Balbás⁵, Antonina Chaban⁵, Raffaella Fontana⁵, Francesca Rosi⁶, Francesca Sabatini⁶, Laura Cartechini⁶, Brenda Doherty⁶, Letizia Monico⁶, Mixon Faluwiki⁷, Patrick Atkinson⁷, Chi Shing Cheung⁷, Haida Liang⁷, Joshua A. Hill⁷, Donata Magrini⁸, Georgios Karagiannis⁹, Stamatios Amanatiadis⁹, Joen J. Hermans^{1,2} & Katrien Keune^{1,2}

Long-term condition monitoring of works of art can provide new insights into object-specific deterioration mechanisms. Detecting change over time allows us to determine whether deterioration is active, to investigate its cause and to establish the efficacy of conservation interventions. However, long-term condition monitoring poses both logistical and technical challenges. To address the latter, a 6-month pilot study using model systems has been performed to investigate the approach to long-term monitoring of chemical dynamic processes in oil paintings. The focus was placed on metal soap protrusions: a condition phenomenon encountered in oil paintings that results from dynamic chemical pigment-binder interactions. Eight portable non- or minimally invasive examination technologies available via the MOLAB facility of IPERION HS were used to detect change in model systems. These model systems were designed to form lead soap protrusions in situ in a short time frame by including reactive components in their stratigraphy, providing changes on a scale more typical of years or decades in real paint systems. Raking light imaging or commercial colorimetry did not provide sufficient resolution for detecting small-scale changes associated with lead soap protrusions. X-radiography with consistent acquisition parameters in combination with a form of automated recognition of protrusions was found to provide a relatively accessible method for monitoring changes in the spatial distribution of protrusions. 3D techniques such as optical coherence tomography and micro-profilometry were found to be suitable for detecting change in lead soap protrusions, provided that they reach sufficient spatial resolution in the plane of a paint layer ($\leq 20\ \mu\text{m}$) and depth ($\leq 2\text{--}3\ \mu\text{m}$). Acoustic microscopy was found to provide insufficient spatial resolution for this purpose. More specificity for lead soaps was provided by techniques that couple high resolution 2D or 3D imaging to spectral information, such as micro-profilometry coupled to VIS-NIR spectroscopy.

Long-term condition monitoring is an integral part of a proactive approach to conservation of works of art¹. Monitoring goes beyond detection and localisation of condition phenomena. Long-term monitoring involves recording condition phenomena over time in a systematic manner to produce comparable observations². Detecting change is necessary to

understand whether deterioration is actively occurring and to identify its cause. Furthermore, detecting change allows us to evaluate the efficacy of interventions so that we can learn from past and current care practices³. When changes are identified before they become apparent on the surface of the work of art, i.e. detected sub-surface, they can function as early warning

¹Conservation and Science Department, Rijksmuseum, Hobbemastraat 22, 1071 ZC Amsterdam, The Netherlands. ²van 't Hoff Institute for Molecular Sciences, University of Amsterdam, Science Park 904, 1098 XH Amsterdam, The Netherlands. ³Institute of Physics, Faculty of Physics, Astronomy and Informatics, Nicolaus Copernicus University in Toruń, Ul. Grudziadzka 5, 87-100 Toruń, Poland. ⁴Faculty of Fine Arts, Nicolaus Copernicus University in Toruń, Sienkiewicza 30/32, 87-100 Toruń, Poland. ⁵CNR-INO, National Institute of Optics, (National Research Council of Italy), Largo Enrico Fermi 6, 50125 Florence, Italy. ⁶CNR-SCITEC, Institute of Chemical Sciences and Technologies "Giulio Natta", (National Research Council of Italy), Via Elce di Sotto, 8 06123 Perugia, Italy. ⁷School of Science & Technology, Nottingham Trent University, Nottingham, NG11 8NS, UK. ⁸CNR-ISPC, The Institute of Heritage Science, (National Research Council of Italy), Via Madonna del Piano 10, 50019 Sesto Fiorentino, Italy. ⁹Ormylia Foundation, 63071 Ormylia Halkidiki, Greece. ✉e-mail: j.r.duivenvoorden@uva.nl

signs. Currently, heritage institutions across the world are in the process of redefining their indoor climate conditions⁴. As it is an open question whether there are any long-term implications for the stability of the collection, now is an opportune moment to start long-term monitoring to collect data on the environmental response of collections.

Several practical and technical challenges are associated with monitoring, particularly when carried out over a long period of time. There are logistical challenges, for example ensuring repeated access to the work of art and monitoring instrumentation, sustainable data management, and continuity in monitoring methods when staff and instruments change over time. In this work, we focus instead on the technical challenges regarding long-term monitoring. Whilst short-term monitoring of the effects of treatment is employed regularly in the conservation of paintings^{5–8}, few formal, i.e. planned and systematic, long-term condition monitoring projects have been carried out so far, except for condition monitoring in the built heritage environment^{9,10}. Although re-assessment of objects after several years to evaluate intervention efficacy is common in conservation practice, it is generally done on an ad hoc basis¹¹. We refer to long-term monitoring when a significant amount of time, e.g. weeks or years, passes between successive measurements, which increases the risk of variation in experimental setup or measurement conditions. Typically, the total duration of long-term monitoring is in the order of decades.

Many deterioration phenomena in oil paintings are associated with dynamic chemical processes, for example pigment alterations^{12–14}, liquifying of binding medium^{15,16} and pigment–binder interactions such as metal soap formation, the topic of this paper. Metal soaps result from saponification of oil paint, a reaction between metal ions originating from pigments or additives and free fatty acids in the oily binding medium^{17–19}. Sometimes, metal soaps were intentionally added to modern oil paints during manufacturing²⁰, but more often, their appearance in works of art is due to chemical change over time. Metal soaps are found in paintings in different manifestations, such as efflorescence, surface crusts, increased paint transparency, and protrusions^{21–23}. Protrusions are aggregated metal soaps generally between 10–500 µm in diameter that, when formed at depth, push through the paint layers towards the surface^{22–25}. While the formation of metal soaps can also have a stabilising effect on oil paints, protrusions are generally considered to be causing unwanted structural and aesthetic changes to paint layers²⁶. Despite our general understanding of metal soap protrusions, many questions remain open, for example regarding the conditions that favour protrusions over other metal soap manifestations. Similarly, it is not well understood how sensitive metal soap protrusions are to environmental influences and remedial treatments. Monitoring metal soap protrusions in affected paintings over the long term could contribute to answering such questions and support preventive and remedial conservation decision-making.

In this paper, we explore technical challenges associated with long-term monitoring of metal soap protrusions that were encountered in Task 5.1 (‘Methodological and instrumental developments for preventive conservation’) of the EU-funded project Integrating Platforms for the European Research Infrastructure ON Heritage Science (IPERION HS). Within this task, a research consortium of six partners performed a pilot study in which model systems were used as tools to evaluate non- or minimally invasive monitoring techniques. The model systems were specifically designed to be highly dynamic in a short time frame. The concept of the dynamic model systems has previously been proved to be successful for in-situ lead soap formation in a matter of months^{27,28}. The model systems are multi-layered systems that simulate a typical Old Master painting stratigraphy, consisting of a sized canvas, a chalk–glue ground layer, and an oil paint layer with iron oxide or smalt pigment. These pigments were selected to obtain an opaque (iron oxide) and translucent (smalt) paint layer. In between the ground and the paint layer a so-called ‘active’ layer was added that was composed of reactive components with the specific aim to form lead soap protrusions over several weeks. The non-invasive analytical techniques employed in this pilot study are all part of the suite of techniques offered in the transnational

Mobile Laboratory (MOLAB) facility offered within the catalogue of services of the IPERION HS framework, which will be continued in the European Research Infrastructure for Heritage Science (E-RIHS) framework²⁹. The model systems were prepared at the Rijksmuseum and sent to six partners of the IPERION HS consortium where they were kept under constant conditions for a monitoring experiment of six months. Changes in three different properties related to lead soap protrusions were followed over time: chemical properties of the protrusions, visual appearance of the model systems and structural properties of the protrusions.

This paper starts by discussing the analysis of samples taken from the model systems, to characterise the systems and the protrusions. Following the cross-section analysis, the results of the non- or minimally invasive monitoring will be discussed, beginning with the monitoring of chemical changes using external reflection Fourier-transform infrared (FTIR) spectroscopy. External reflection FTIR is routinely employed for the in-situ investigation of metal soaps^{30–33}. Next, three relatively accessible techniques will be discussed: raking light photography (RL) and colorimetry which provide information about the visual appearance of the model systems, and X-radiography, which has been successfully employed to detect and localise protrusions in works of art²⁴. Also, a photography-based technique with automated recognition has been used before to detect metal soap protrusions in paintings²⁵. The results of these techniques will be compared to high-tech imaging techniques that are able to capture the structure of the protrusions in three dimensions: optical coherence tomography (OCT), acoustic microscopy and micro-profilometry. OCT, too, has been employed to detect and localise protrusions in oil paintings^{34,35}. As the monitoring was not performed on the same set of model systems the primary goal of this study is not to compare the observed trends between the different techniques. Instead, we aimed to test the suitability of the techniques and data analysis approaches for the quantitative monitoring of lead soap protrusions in painted model systems with different chemico-physical characteristics. The ultimate goal of this pilot study is to inform and explore non- or minimally invasive monitoring approaches in preparation for the implementation of long-term monitoring of paintings in museum collections, such as Rembrandt’s *The Night Watch* (1642) at the Rijksmuseum, Amsterdam. This painting is the subject of a large-scale research and conservation project called *Operation Night Watch* and suffers from lead soap protrusions³⁶. The findings we present may guide others in designing long-term quantitative condition monitoring in collections.

Methods

Model system preparation

A linen canvas (80 × 60 cm, Van Beek Art Supplies “Antwerp” 220 g/m²) stretched onto a wooden stretcher was sized twice with 8% w/v rabbit skin glue (Gerstaeker). The canvas was further prepared with a calcium carbonate–animal glue ground, applied in three layers with a broad brush. The ground consisted of 100 g Champagne chalk (CaCO₃, Gerstaeker) which was added to 200 mL 4% rabbit skin glue solution while stirring. Next, the ‘active layer’ was applied. This layer contained 1.0 g margaric acid (3.70 mmol) (heptadecanoic acid, 98%, Alfa Aesar), 1.0 g (2.64 mmol) lead (II) acetate trihydrate (Merck) and 8 mL cold-pressed linseed oil (de Kat). The margaric acid was dissolved in acetone before adding to the linseed oil. The lead acetate was ground in a mortar with a pestle. After the acetone was left to evaporate from the linseed oil mixture, the lead acetate was added and briefly mixed with a palette knife. The mixture, which became viscous upon adding the lead acetate, was applied onto the prepared canvas with a drawdown bar (wet thickness 50 µm). Four days later, two different types of paint layers were applied on top of the active layer, applied with the drawdown bar (wet thickness 100 µm). A paint layer containing smalt was prepared by grinding 2.5 g smalt (de Kat, 0.212–0.300 mm particle size) in 2 mL linseed oil with a glass muller on a glass slab for 20 min. A second batch of smalt oil paint was prepared in the same manner with 1.3 g smalt in 1 mL linseed oil. A paint layer containing iron oxide was prepared by grinding 4.0 g red iron oxide (120 M, synthetic iron oxide >3 nm, Kremer Pigmente) to 4 mL linseed oil. These two types of pigments were chosen to create one

Table 1 | Monitoring dates

Time label	Week	Date
T0-Active layer application	–	07 Feb 2022
T0-Paint layer application		11 Feb 2022
T1	1	21 Feb 2022
T2	2	28 Feb 2022
T3	3	07 Mar 2022
T4	4	14 Mar 2022
T5	5	21 Mar 2022
T6	6	28 Mar 2022
T7	7	04 Apr 2022
T8	8	11 Apr 2022
T9	12	09 May 2022
T10	16	06 Jun 2022
T_{end}	31	19 Sep 2022

opaque and one translucent paint layer. Small pieces ($\pm 2 \times 2$ cm) were cut from the canvas three days later, while the paint was still sticky. Carefully pinned onto a composite board and wrapped in plastic zip lock bags, the model systems were sent to all partners. In addition to a smalt and iron oxide model system, each partner also received reference pieces of plain sized canvas, sized canvas with the ground, and sized canvas with the ground and active layer.

Parallel cross-section analysis of the model systems

Parallel to the non- or minimally invasive monitoring of changes in the model systems, cross-sections were prepared of samples from the model systems to characterise the chemical process of lead soap formation. The cross-sections were analysed with a combination of microchemical imaging techniques: light microscopy, scanning electron microscopy with energy dispersive X-ray analysis and micro-attenuated total reflection Fourier-transform infrared spectroscopy. In addition, the active layer was analysed using bulk attenuated total reflection Fourier-transform infrared spectroscopy. Finally, the surface of the model systems was scanned using micro-external reflection Fourier-transform infrared spectroscopy. The details of the cross-section analysis and the micro-imaging instrumentation are listed in the Supporting Information (henceforth SI) section S1.1.

Monitoring conditions

After distribution, the model systems were stored in the dark at 30 °C and 50% relative humidity (RH) using a saturated solution of magnesium nitrate hexahydrate. Variation in conditions in the different laboratories was reported (RH between 46 and 60%, T between 27.5 and 30 °C). The model systems were removed periodically for analysis. In the first seven weeks of the monitoring campaign (21 February to 4 April 2022), measurements were performed weekly (T1–T7). From week eight onwards, the measurements were performed monthly for the next three months (May, June, July) (T8, T9, T10). The final measurement was performed mid-September (T_{end}), see Table 1 for the precise monitoring dates. The dates in bold were used for data analysis, as they represented the time points with most complete sets of analyses.

External reflection Fourier-transform infrared spectroscopy

External reflection FTIR spectroscopy in the mid-IR range is a surface technique and depending on the optical geometry and surface optical properties, the first few microns (less than 10 µm) are probed. Measurements were performed with a compact, portable FTIR spectrometer (ALPHA, Bruker Optics, Germany/USA—MA) that is equipped with a SiC Glowbar source, a RockSolid™ interferometer with gold mirrors and a DLaTGS detector. All data were collected using Opus software (v7.2). The optical layout of the external reflectance module is 22°/22°. Pseudo-

absorption spectra ($\log(1/R)$; where R = reflectance) were acquired from areas of about 20 mm², using 144 scans in the spectral range of 7000–375 cm^{−1}, at a spectral resolution of 4 cm^{−1}. Spectra collected from a flat gold mirror were used as background. Three spectra were acquired on different areas of the sample.

Colorimetry

A spectrophotometer (Konica Minolta mod. Chroma Meter CM-700d) registered the colour coordinates L*, a* and b* on selected areas (5 mm in diameter) for each monitoring step. Colour measurements were performed with standard illuminant D65 and observer 10° (EN15886 2010) following the standardised method CIELAB 1976. The calibration against a SPECTRALON® white reference was performed before any measurement. Each colorimetric value (L*, a*, b*) was the auto-averaging of three subsequent measurements. Measurements were taken on the same locations on the model system surface by using a transparent mask to indicate the areas. The colour coordinates of each specimen corresponded to the mean value of five measurements. Colour distance ΔE values were calculated according to Eq. 1.

$$\Delta E = \sqrt{(\Delta L)^2 + (\Delta a)^2 + (\Delta b)^2} \quad (1)$$

Multispectral colorimetry coupled to micro-profilometry

Colorimetric coordinates (L*a*b*) were calculated from the visible range of the reflectance spectra measured with a multispectral visible to near-infrared (VIS-NIR) scanner, developed in-house at the Italian National Institute of Optics³⁷. The procedure for the extraction of the colorimetric data has been published elsewhere³⁸. The VIS-NIR scanner acquires, in a point-by-point modality, the backscattered light from a surface with a spatial sampling of 250 µm (~4 point/mm), generating 32 monochromatic images in the visible (from 380 to 780 nm) and in the infrared region (from 790 to 2500 nm) with a spectral sampling step of 20–30 and 50–100 nm, respectively. The constant motion of the optical head, which acquires a single point in circa 1 ms, prevents the surface of the painting from being heated significantly. The instrument works at 12 cm distance from the surface in a 45°/0° (illumination/detection) configuration according to CIE standards. The system is operated through a custom-developed software, with simultaneous control of the movement of the scanner head, autofocus and image acquisition. The CIELAB 1976 colour-space and D65 illuminant with observer at 2° were used. L*a*b* coordinates are reported as average values related to the entire area of the model system (30 × 30 mm²) or to a specific region of interest. ΔE values were calculated according to Eq. 1. The pixel size of the acquired VIS-NIR images is 250 × 250 µm². Only the monochromatic images in the visible light range were considered for calculation of the colorimetric coordinates.

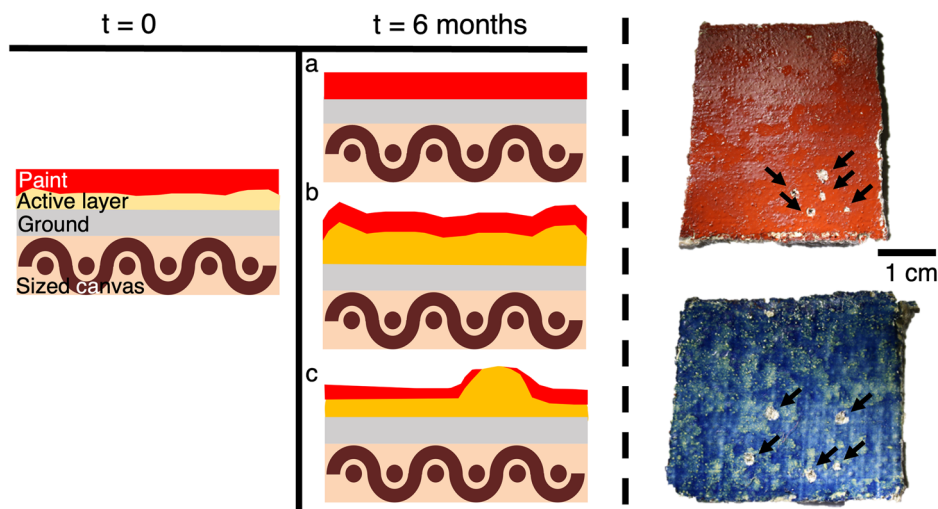
Raking light photography

Raking light (RL) images were taken using a modified Canon EOS 7D (18 megapixels, CMOS sensor) camera body, operated in manual mode. The lens used was a Canon EFS 18–135 mm f/3.5–5.6 IS mounted with a B + W 468 UV/IR cut filter. The flashes were positioned at approximately 30 cm distance and at an angle of 10° to 30° relative to the plane of the model system surface. Data analysis was performed in ImageJ.

X-radiography

The model systems were imaged in transmission using a Balteau Baltograph X-ray system (Baltograph generator XSD225 with X-ray tube TSD225/0). Tube settings: 32 kV; 2.5 mA; focal spot size 1 mm (640 W); dwell time 60 s; X-ray source and image plate distance 112 cm. The image plate (resolution 25 µm) was scanned using a Duerr HD-CR 35 NDT CR-scanner. Midway through the monitoring period, the X-ray tube was replaced (Comet MXR-320HP/11) due to planned maintenance. The X-radiographs were analysed using the Analyze tools in ImageJ³⁹.

Fig. 1 | Left: Model systems containing an active layer with reactive components to form lead soap protrusions in situ in a short time frame. Right: Photographs of the model systems with smalt and iron oxide oil paint. Arrows indicate locations where materials were sampled.



Optical coherence tomography

Two OCT setups with different wavelengths have been employed in this study, 850 nm and 1300 nm. The 850 nm OCT setup was developed in-house at the Institute of Physics, Nicolaus Copernicus University in Toruń, Poland, as a portable instrument for the examination of cultural heritage objects. The 850 nm OCT instrument contains a broadband (770 nm–970 nm) source (Broadlighter Q-870-HP, Superlum, Ireland) and a spectrograph (Cobra CS800-840/180 spectrometer, Wasatch Photonics, USA) as a detector. The instrument is fitted with a telecentric lens (LCM04 from Thorlabs, $F = 54$ mm) and two HR CCD cameras to precisely annotate the examination spot. The lateral resolution is 13 μm and the axial (in-depth) resolution is ca. 2.2 μm (in paint) and 3.2 μm (in air). The distance to the object examined is 43 mm. In this study, an area of 12×12 mm² of the model systems was scanned and a data cube of $4000 \times 150 \times 1024$ voxels (x , y , z) was acquired in approximately 30 s with a voxel size of $3 \times 80 \times 1.85$ μm^3 (x , y , z). From this data B-scans (cross-sectional brightness scans) were extracted and presented in false colour scale: strong scattering areas are shown in warm colours (red to yellow), low scattering ones in cold colours (green to blue) whereas areas not scattering light or not accessible as black. The position of the air-paint boundary was extracted from the same data cube. The resultant surface maps were interpolated ten-fold in y -direction to reach 4000×1500 pixels or 3×8 μm^2 pixel size. A detailed instrument description with standard post-processing procedures for the visualisation of cross-sections has been published elsewhere⁴⁰.

The OCT measurements at 1300 nm were performed with a Thorlabs Telesio II system. The axial resolution was 5.5 μm in air and 3.7 μm in paint, although the practical resolution was lower due to strong sidelobes. The lateral resolution was 13 μm . Cubes of $500 \times 500 \times 1024$ voxels (x , y , z) were collected with a voxel size of $20 \times 20 \times 3.48$ μm^3 (x , y , z). The sampling resolution was chosen to be worse than the optical resolution as a trade-off between the field of view and image cube size limited by the PC's RAM. The A-scan (depth profiles) frame rate was 76 kHz resulting in a B-scan capture time of 7 ms.

Laser scanning interferometric micro-profilometry

Laser scanning interferometric micro-profilometry was performed with a device built in-house at the Italian National Institute of Optics⁴¹. It is based on a distance meter (655 nm, ConoPoint-10, Optimet, Jerusalem Israel) with a 25 mm lens mounted on an XY scanning system. To create a constant positioning reference system for the 3D measurements at different times and to minimise the deformation of the canvas, the model systems were fixed to a wooden panel with epoxy resin (a small amount placed in the corners of the samples). Anchored samples were then positioned vertically in front of the micro-profilometric scanning system. The scanned areas

(45×50 mm²) were acquired with a 20 μm lateral step size at a 3 μm resolution in depth. The laser (655 nm wavelength) is focused to approximately 27 μm spot size and power set to 0.17 mW for the iron oxide model system and 0.78 mW for the smalt model system. The data was processed with in-house software.

Acoustic microscopy

Acoustic microscopy measurements⁴² were taken using a 175 MHz piezoelectric transducer (Panametrics-NDT model V3965) and an analogue-to-digital converter (Acquisition Logic Data Acquisition card AL8xGT 2.0) with 1 G sample/s sampling rate. The area of investigation was approximately 15 mm². The lateral resolution of the setup used here was 50×50 μm^2 and the depth resolution was approximately 20 μm . An ultrasonic hydrogel (Aquasonic 100) was applied to the surface of the model systems as a transmission agent and gently removed after every measurement using a damp cloth.

Results

Cross-section analysis of model systems to contextualise non-invasive monitoring

The model systems and the lead soap protrusions were characterised by micro-invasive techniques parallel to the non-invasive monitoring. First of all, following the reaction between the two reactive components in the active layer, lead acetate trihydrate (PbAc) and heptadecanoic acid (FA17) in a separate experiment, it became clear that lead soaps likely already formed during the mixing of the active layer (S1.2 in the SI). The monitoring data at T1, 2 weeks after the application of the active layer, showed that the surface of the model systems at that point already experienced protrusions-like deformations. This is well visible in the raking light images (Fig. 6). In the absence of monitoring data before T1 no conclusions can be drawn about the early-stage development of the protrusions.

The cross-sections indicated that the model systems roughly evolved into three forms. An overview of all cross-sections can be found in section S1.3 in the SI. In the areas without protrusion-like formations (first form), the active layer is not or minimally visible under the microscope or in the backscattered electron (BSE) images (Fig. 1a and Figs. S2, S3 in section S1.4), suggesting that lead-rich components are less present here. In other areas (second form), the active layer expanded in size without forming protrusion-like structures (Fig. 1b). In the third form, protrusion-like aggregations formed (Fig. 1c). Overall, the protrusion-like structures varied in size between approximately 100–500 μm at approximately 0–50 μm in depth. The concentration of lead soaps in the active layer varies. Examples were found of a thickened layer or protrusion-like structures in which the bulk of the material was oil-like and contained only small, localised domains

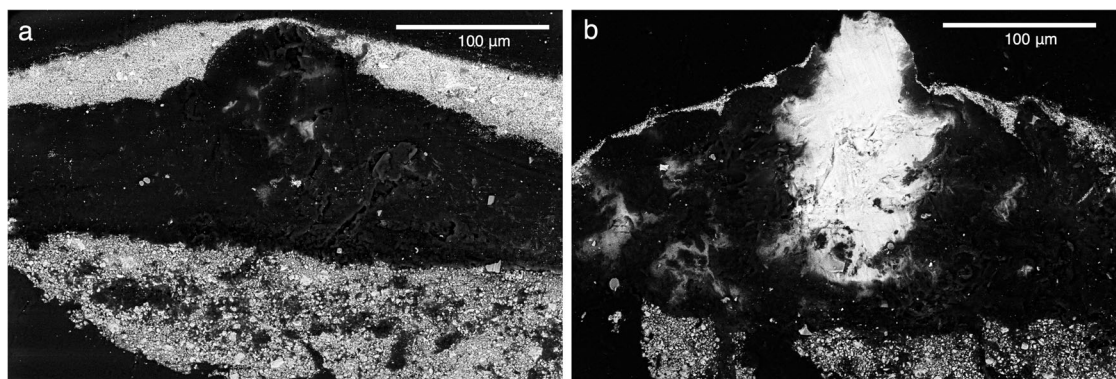


Fig. 2 | BSE images of cross-sections of protrusion-like structures sampled from the model system with iron oxide oil paint layer. a Sample taken at T1. **b** Sample taken at T7.

of lead soaps (Fig. 2a). On the other hand, examples of higher concentrations of lead-containing structures were also encountered that, in some cases, even broke through the paint surface (Fig. 2b).

μ -ATR-FTIR analysis on the cross-sections confirmed the observation that the lead soap concentration varies. Smearing of the embedding medium due to a short drying time was visible on the surface of all cross-sections. The lead soap domains in two cross-sections taken at T1 and T3 are small (Figures S4, S5 in section S1.5), in the order of a few micrometres to several tens of micrometres. Figure 3 shows an example of a cross-section taken in the final week (week 31, T_{end}) of the monitoring campaign of the model system with an iron oxide paint layer. Here, the lead soap domain is larger, around 200 μm in diameter. The infrared spectrum extracted from an area of lead soaps (Fig. 3d) shows a crystalline structure (sharp $\nu_s(\text{CH}_2)$ at 2848 cm^{-1} , sharp $\nu_a(\text{CH}_2)$ at 2916 cm^{-1} , sharp $\nu_a(\text{COO}^-)$ doublet at 1510 and 1536 cm^{-1} , distinct $\delta(\text{CH}_2)$ zig-zag pattern between 1186 and 1340 cm^{-1})¹⁹. Due to the limited number of cross-sections and the local information they provide, it is not possible to make conclusions about how the lead soaps evolve over time. It is clear, however, that we can observe variations in the shape and thickness of the active layer and the size and degree of crystallinity of the lead soap domains within the active layer.

Monitoring chemical changes with external reflection FTIR

External reflection FTIR was used for non-invasive detection of lead soaps. The external reflection FTIR spectra for the iron oxide and smalt model systems at time points T1, T3, T8 and T_{end} are visible in Fig. 4. In both model samples, the main features are due to the bands of linseed oil ($\nu + \delta(\text{CH})$, $\nu(\text{CH})$, $\nu(\text{C}=\text{O})$ and $\nu(\text{C}-\text{O})$) and calcium carbonate from the ground layer (at 2500 cm^{-1}). The lattice mode ($\text{Fe}-\text{O}$) is present in the spectra acquired on the iron oxide samples (Fig. 4a), while the silicate components ($\nu(\text{Si}-\text{O})$ and $\delta(\text{Si}-\text{O})$ at about 1080 and 470 cm^{-1}) are observed in the smalt samples (Fig. 4b). The FTIR spectra do not clearly highlight the presence of spectral features due to crystalline lead carboxylates characterised by the typical sharp $\nu(\text{COO}^-)$ band in the range 1500–1560 cm^{-1} . Only at the longest ageing time in the iron oxide sample (T_{end}) the COO^- stretching region shows an inverted band (at about 1510 cm^{-1}) that could be assigned to crystalline lead soaps (Fig. 4a).

To evaluate the effect of the lateral resolution on lead soap detection by the portable external reflection FTIR, the iron oxide model system was also analysed with external reflection FTIR on the micro-scale. A benchtop FTIR microscope with a Focal Plane array (FPA) detector was used to achieve a chemical mapping of the surface at the microscale at T8 and T_{end} . At T8, external reflection micro-FTIR imaging reveals the presence of crystalline lead carboxylates as small nuclei (10 μm) and larger agglomerates (not exceeding 30–40 μm), while macro-FTIR spectroscopy did not detect crystalline lead soaps (Figure S6 in section S1.6). Similarly, at T_{end} micro-FTIR imaging indicates the presence of lead carboxylates as agglomerates with variable micro-scale dimensions (not larger than 60–70 μm) (Fig. 5), even

though the macro-FTIR setup only shows a hint of the signal assignable to lead carboxylates.

μ -ATR-FTIR imaging on the cross-sections (Fig. 3 and section S1.5 in the SI) supports the observations made with external reflection micro-FTIR imaging. Multiple examples of small (several micrometres to several tens of micrometres in diameter) crystalline lead soap domains were encountered in the cross-sections, alongside larger crystalline domains. The μ -ATR-FTIR study further evidences the variability of crystalline lead soap domain distribution along the stratigraphy, not always present at the very near surface and thus not detectable by non-invasive FTIR spectroscopy sensitive to the first superficial microns. Furthermore, the sampled area by the portable FTIR system using the smallest pinhole is around 3 mm (diameter size) and the dimensions and number of the newly formed lead carboxylates are too small to be revealed by the macro-FTIR setup. The signals from the sampled area are mainly due to the paint matrix covering the carboxylate bands associated with the micrometre-size lead soap agglomerates.

Monitoring protrusion distribution using raking light photography

Raking light (RL) photography was performed to assess the suitability of this low-tech imaging technique for protrusion monitoring. A region of interest was selected manually for all RL images and converted to 8-bit greyscale. The histogram was normalised, and pixels were selected based on their greyscale value. Two thresholds were compared: grayscale values >200 and >250 (out of 256). Figure 6 shows the results of this analysis for the smalt model systems. It became clear that dust on the surface, differences in lighting conditions, heterogeneity of the paint layer and the canvas structure heavily impacted the analysis. Particularly in the case of the iron oxide systems, heterogeneity in the gloss of the surface made the quantification unreliable. See Figure S7 in section S2.1 in the SI for the RL images of the iron oxide model system.

Monitoring protrusion distribution using X-radiography

X-radiography was employed to monitor the elemental distribution of lead in the model systems. As the contrast in X-ray absorption between the lead-containing areas and the surrounding material was better in the smalt model systems compared to the iron oxide model systems, the results of the smalt system were analysed further. Additional information about the X-radiography can be found in S2.2 of the SI. As maintenance of the instrumentation prevented measurement from being taken for the entire length of the experiment, only two time points are compared as an illustration of the potential of this technique (Fig. 7). Because the differences in distribution between the two time points are small, the number and size of the lead-containing areas were analysed using an automated approach. The contrast of the X-ray photographs was enhanced by normalising the histogram (Fig. 7a, b), followed by the isolation of high-intensity pixels using a greyscale threshold (Fig. 7c, d). These pixels were interpreted as lead-containing areas. Analysis of these pixels revealed that the area covered by lead-based materials stays constant over this time (1.7% of the total area);

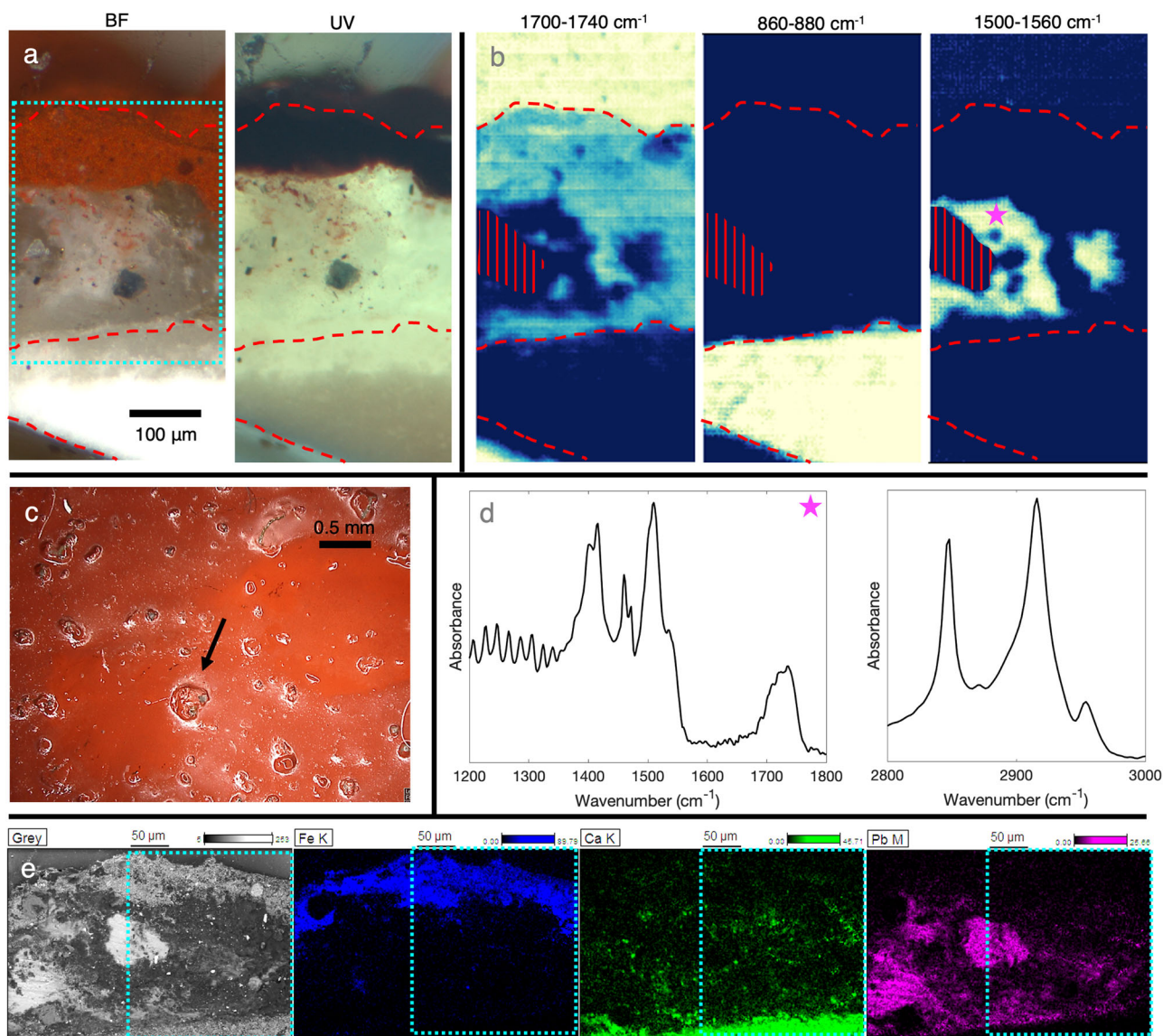


Fig. 3 | Cross-section of iron oxide model system. Sample taken in week 31 (T_{end}). **a** Visible and UV light microscopy. Red dashed lines indicate the layers of the stratigraphy. **b** μ -ATR-FTIR maps, analysed with PyMCA⁴⁵. The wavenumber range 1700–1740 cm^{-1} corresponds to the ester vibration band. High intensity (yellow) corresponds to the embedding medium and lower intensity (blue) corresponds to the ester of oil. Red vertical hashed lines indicate insufficient contact between the

sample and the ATR crystal. 860–880 cm^{-1} range corresponds to a carbonate vibration band of calcium carbonate (in the ground layer). 1500–1560 cm^{-1} range corresponds to the lead carboxylate vibration band of lead heptadecanoate.

c Sampling location. **d** ATR-FTIR spectrum extracted from the area in the μ -ATR-FTIR carboxylate map indicated with a star. **e** SEM-BSE image and EDX elemental maps of Fe-K, Ca-K, and Pb-M. The blue dotted box corresponds to the area in (a).

however, the number of isolated areas goes down (1019 to 841), and size distribution shifts towards higher values (Fig. 7g). These numbers suggest that the lead-based materials are aggregating.

Monitoring colour change using colorimetry

The third technique considered relatively accessible is colorimetry using the commercially available spectrophotometer. It was hypothesised that the formation and growing of lead soap protrusions could lead to a colour change related to the thinning or disruption of the paint layers. As it was not known beforehand which colour coordinate would be most sensitive to this change, we report here on the total colour difference (ΔE). The corresponding $L^*a^*b^*$ coordinates are reported in S2.3 of the SI. Figure 8 shows the ΔE values indicating the colour changes in the model systems. The superficial heterogeneity and roughness of the model systems lead to high standard deviation values. A strong yellowing of the smalt model systems is registered over the 6-month monitoring period, showing an increase of the b^* coordinate.

The ΔE parameter (CIE 1976) therefore shows significant change over the 6-month monitoring period ($\Delta E > 5$). The yellowing is associated with the yellowing of the oil, not with the growth of protrusions. Cross-section analysis further confirmed that the colour change is not due to colour change of the smalt pigment particles themselves. In the case of the iron oxide model system, the ΔE stays below about 4. For this model system, a slight decrease in L^* over the six months is visible and fluctuating a^* and b^* coordinates. It is not possible to relate these colour changes to protrusion formation or growth.

Monitoring structural changes in three dimensions using OCT

Two OCT systems with different wavelengths were employed to visualise protrusions below the painted surface and monitor changes in their size. The 850 nm OCT system was capable of imaging the smalt model systems down to the ground layer but could not penetrate sufficiently below the surface for the iron oxide model systems. Iron oxide oil paint has low transparency in this wavelength region⁴³. In Fig. S12 in S2.4 a comparison is shown of an 850

Fig. 4 | FTIR spectra recorded in external reflection mode. a FTIR spectra recorded on iron oxide model system. **b** FTIR spectra recorded on smalt model system. Spectra are vertically offset. The expanded spectra in a restricted mid-IR range are also reported (on the right) to highlight the changes that occurred with ageing.

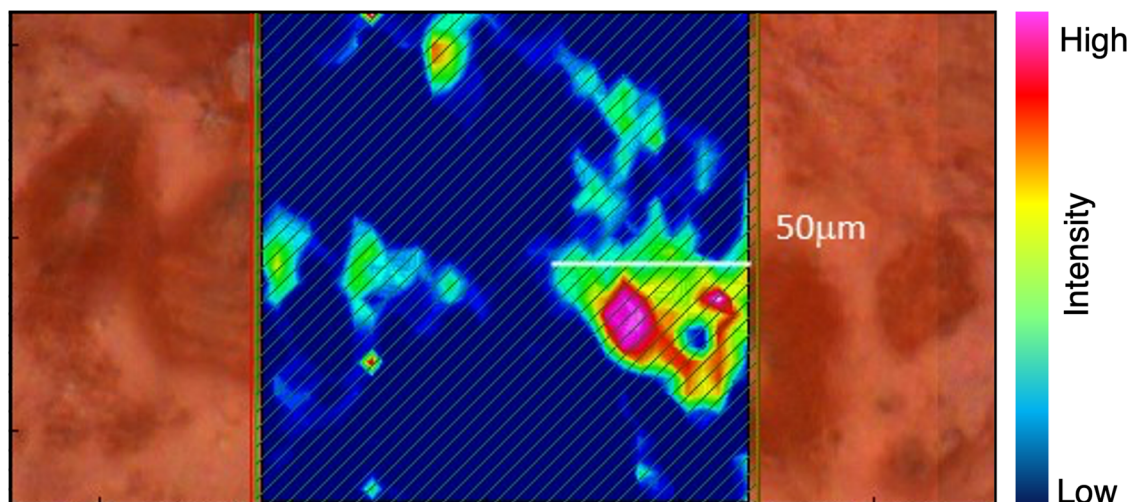
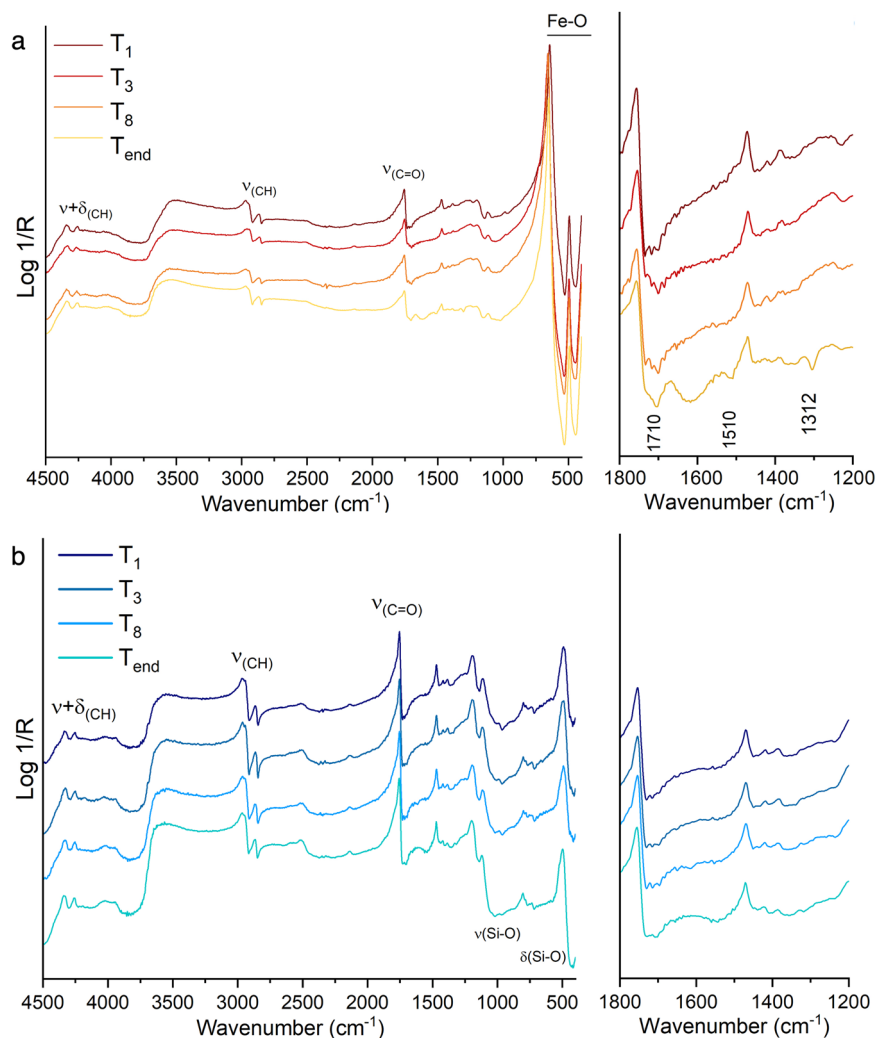


Fig. 5 | External reflection micro-FTIR imaging of the iron oxide model system. The instrumentation is described in S1.1. Example of a chemical image (area dimension 130 × 130 μm²) overlaid onto the visible image, obtained by integrating

the positive peak at 1510 cm⁻¹ at T_{end} . Cassegrain objective 20x (NA 0.6), pixel resolution 2 μm (binned to 4 μm). The approximate dimension of the agglomerate is indicated in the image.

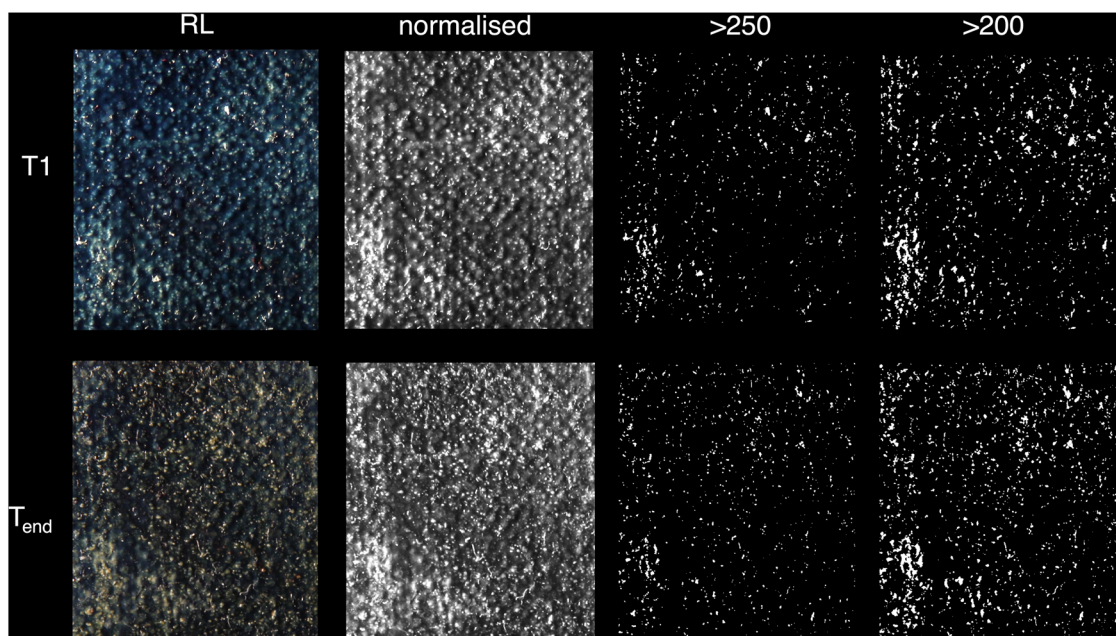


Fig. 6 | From left to right: cropped RL images of the smalt model system at T1 and T_{end}, images resulting from normalised histograms, pixels with greyscale value >250, pixels with greyscale value >200.

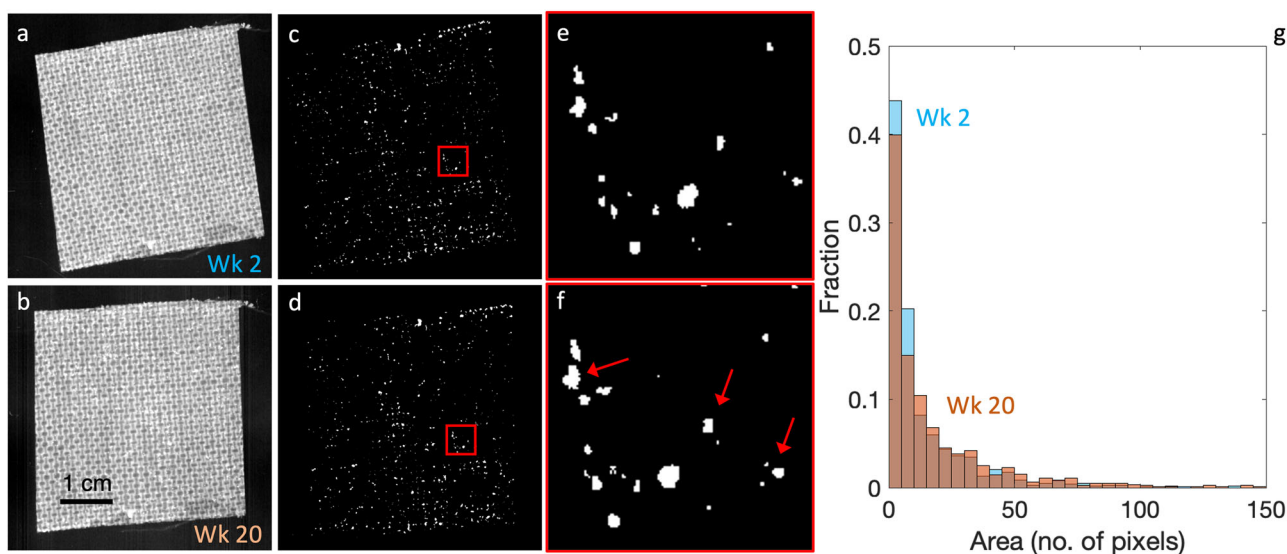


Fig. 7 | X-ray photographs of the smalt model system. **a, b** Normalised 8-bit grayscale image of the model system at week 2 and 20. **c, d** Areas corresponding to lead-based materials isolated by means of a threshold. **e, f** Zoom-in showing details

of the isolated areas. The arrows indicate examples of areas that have changed. **g** Size distribution of isolated areas.

OCT scan to a cross-section taken in the same location. The 850 nm OCT images of the smalt systems revealed the wave-like pattern of the ground on top of the canvas structure and the varying thickness of the ground and paint layers. Figure 9 shows a series of 850 nm OCT cross-section views taken at different monitoring times at the same location on the smalt model system featuring a protrusion that seems to be growing. The protrusions in the model systems appeared as dark areas, as they did not scatter the probing light. Figure S13 in S2.4 shows an example of a manual measurement of the size of a protrusion at T1 and T_{end}. Quantification of this apparent growth is unreliable, due to the low lateral separation of the 850 nm OCT scans in y-direction (80 µm) using the measurement protocol that was followed in this experiment. This could slice the protrusion-like structure differently and obtain a different measure of the dimensions.

The higher lateral resolution of the 1300 nm OCT dataset compared to the 850 nm OCT dataset allowed the assessment of the growth of individual protrusions-like structures (Fig. 10). Due to its longer wavelength, the 1300 nm OCT system was able to visualise the protrusion sub-surface in both the smalt as well as the iron oxide model system. The height or size in vertical direction of each protrusion was considered as the difference between the top (air/protrusion interface) and the bottom of the protrusion (protrusion/paint interface), which is below the painted surface (Fig. 10b, c). Eight protrusion-like structures were selected and isolated based on the 3D surface profile. Figure 10a follows the size of these protrusions over time and shows that there is no strong indication for growth in height. More information about the procedure can be found in S2.5 in the SI.

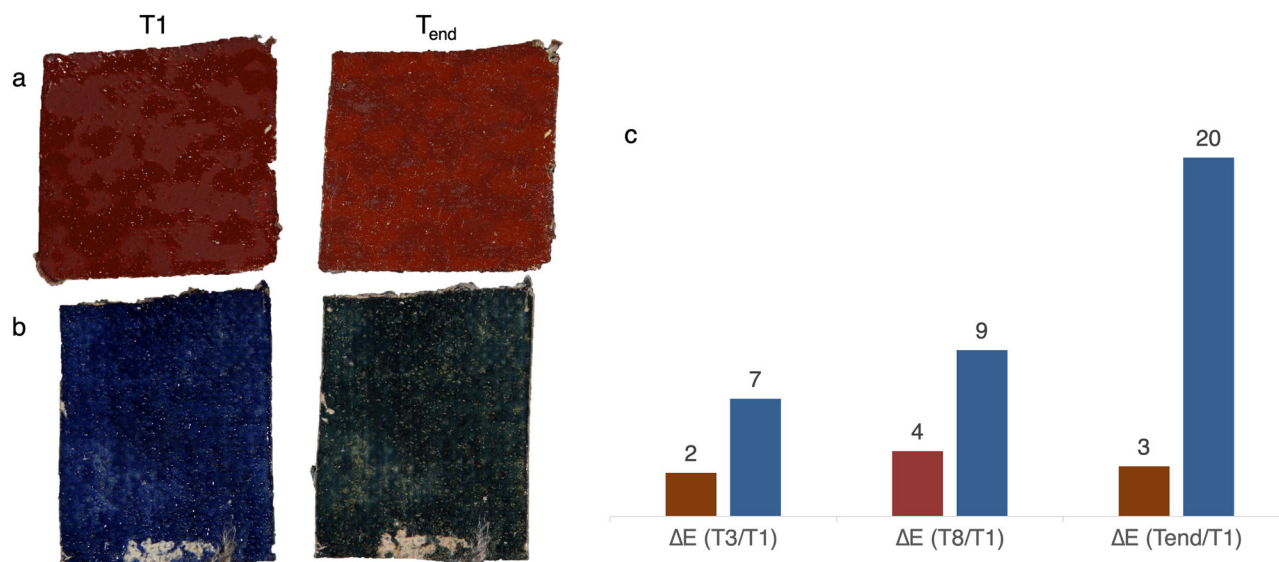


Fig. 8 | Colorimetry on both model systems. **a, b** Photographs obtained from visible light technical photography at T1 and T_{end} of the iron oxide and smalt model systems. **c** ΔE values (CIE 1976) for the iron oxide (in red) and smalt (in blue) model systems compared at T3, T8 and T_{end} compared with T1.

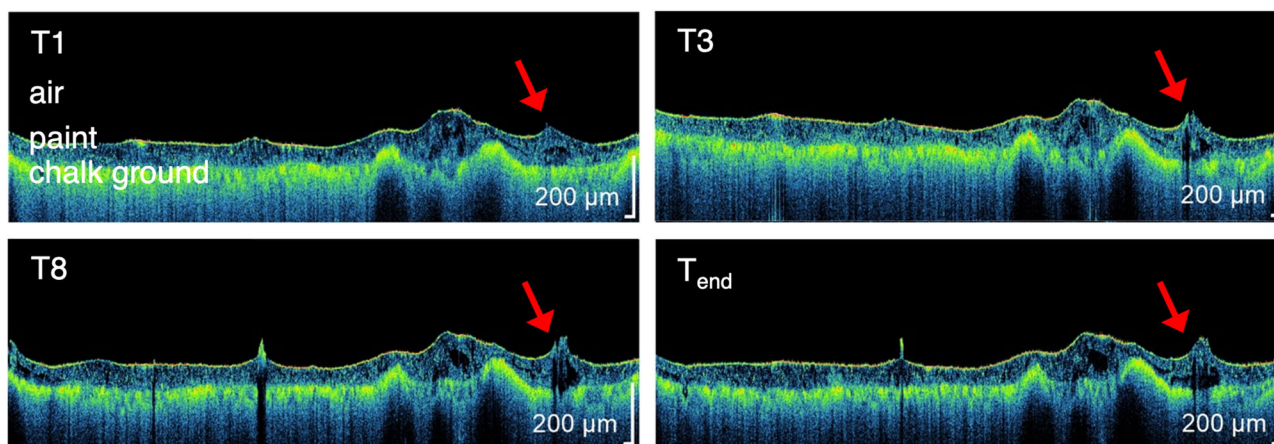


Fig. 9 | Repeated 850 nm OCT line scans of the smalt model system on T1, T3, T8 and T_{end}. Images are corrected for the approximate refractive index of linseed oil, $n_R = 1.5$. The vertical scale is stretched fivefold for better legibility. The red arrow indicates the location of a protrusion.

Acoustic microscopy to visualise sub-surface features of protrusions

Acoustic microscopy was able to visualise and localise protrusion-like structures in the model systems. The technique could penetrate both the smalt and the iron oxide paint layers because acoustic waves can propagate inside many types of materials, including opaque objects. This is in contrast to OCT which is based on electromagnetic waves. However, for acoustic microscopy, a coupling gel has to be applied between the surface and the probe. Therefore, the technique cannot be classified as non-invasive. Figure 11 shows protrusion-like structures in the iron oxide model system, which appeared as dark areas in the scans. The procedure of the acoustic microscopy measurements and scans of the smalt model system can be found in S2.6 of the SI. Both the depth (approximately 20 μm) and lateral resolution (50 × 50 μm²) were not sufficient to quantify the protrusion growth in the acoustic microscopy scans.

Micro-profilometry to monitor changes in the height of individual protrusions

Micro-profilometry produces high-resolution surface maps and was employed to monitor changes in the size of individual protrusions. Micro-profilometry probed the surface with a red laser (655 nm) and created a

surface three-dimensional map. Data acquired from the smalt model systems produced results with a low signal-to-noise ratio due to absorption of the laser radiation by the smalt-containing paint layer. Therefore, only the results of the iron oxide model systems are discussed below. Figure 12 compares two micro-profilometry surface maps of 4 × 4 mm² of the iron oxide model system at T1 and T_{end}. The protrusion-like structures appear as locally raised surfaces, indicated on the maps in red. It is possible to observe several changes in the size and distribution of the protrusions-like structures as indicated in Fig. 12. Below, two approaches to quantifying these changes are discussed.

Similar to the 1300 nm OCT data, the high lateral resolution of the micro-profilometry data allowed the assessment of the height of individual protrusion-like structures above the paint surface—note that this is different from the size of the protrusion in the vertical direction measured above. In Fig. 13, surface profiles at four time points are overlaid at the exact same location to follow the height of two individual protrusion-like structures. Analysis of another coordinate can be found in S2.7 in the SI. Selecting a local baseline proved challenging, as the surface of the dynamic model systems changed rapidly. Baseline correction can strongly impact the measurements, particularly when evaluating changes in the micrometre order. Therefore, Fig. 13 shows the surface profiles that are not locally aligned.

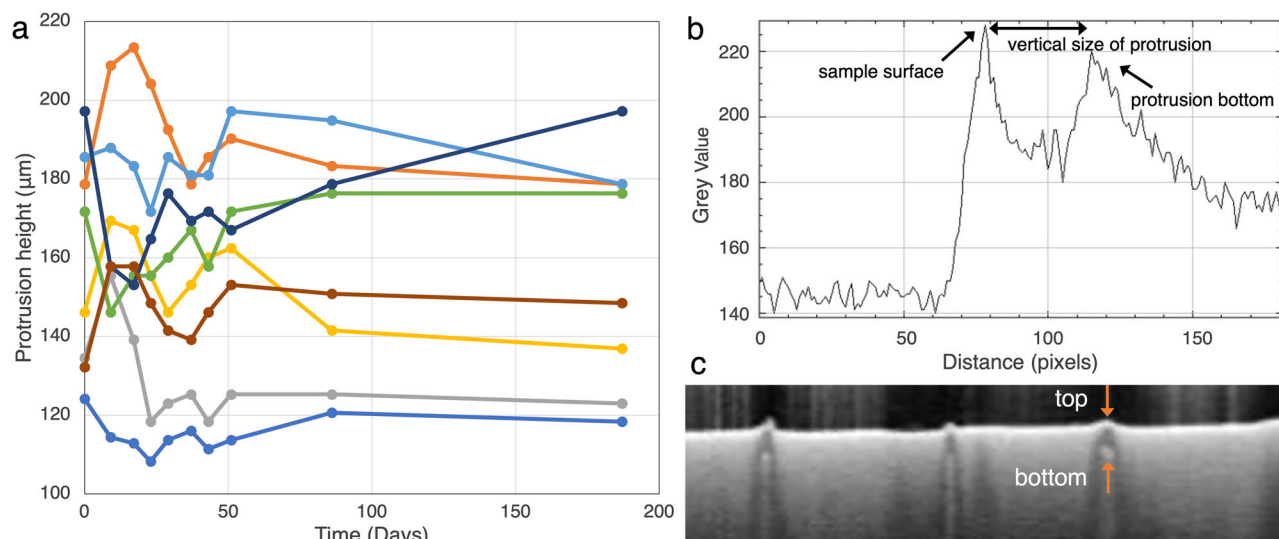


Fig. 10 | Assessment of change in height of eight protrusions based on the 1300 nm OCT analysis of the iron oxide model systems. a Height plotted over time. The height is corrected by the refractive index ($n_R = 1.5$) to give the actual height. **b** The height is defined as the difference between the sample surface and the

bottom of the protrusion-like structure, which is visible here in the depth profile (A-scan). **c** The top and bottom of the protrusion-like structure visible in the cross-section view, image size is 3.9 mm × 0.7 mm.

Fig. 11 | Cross section view of the iron oxide model system at T3 obtained by acoustic microscopy. Protrusion-like structures are indicated by the red arrows.

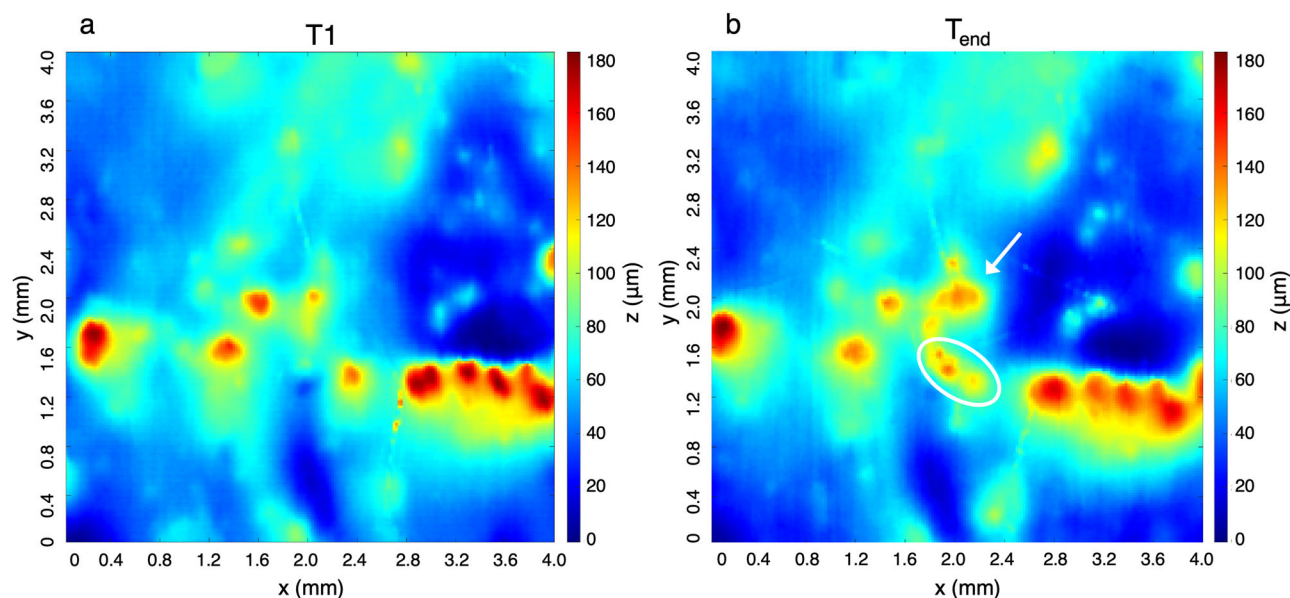
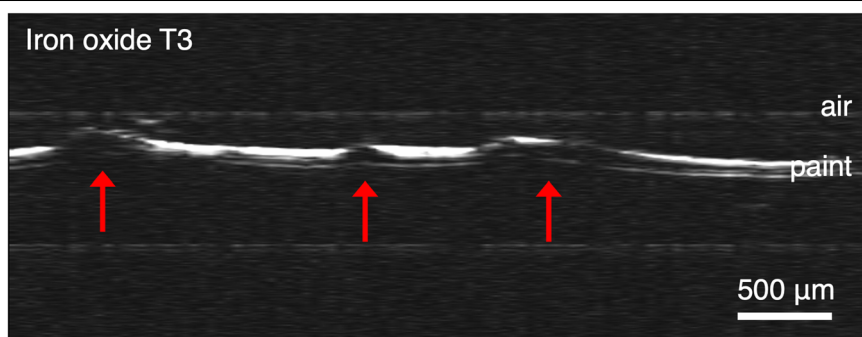


Fig. 12 | 4 × 4 mm² micro-profilometry surface maps of the iron oxide model system of the same area at two points in time. a Map recorded at T1. **b** Map recorded at T_end. The colours indicate the height of the sample (from 0 to 180 μm).

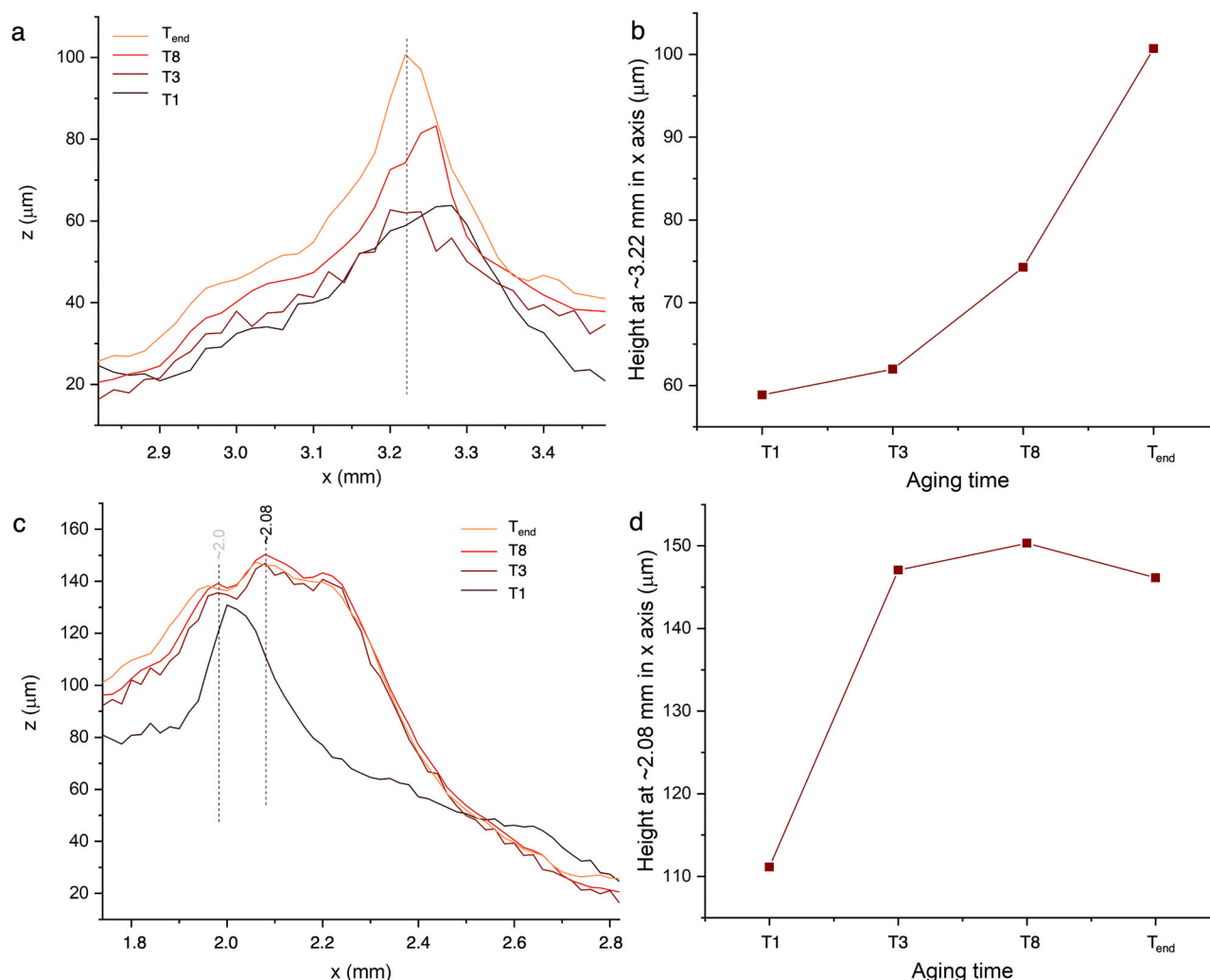


Fig. 13 | Assessment of change in the size of two protrusion-like structures in the iron oxide model system based on micro-profilometry surface profiles. **a, c** Micro-profilometry surface profiles at T1, T3, T8 and T_{end}. **b, d** Absolute height over time.

Monitoring the distribution of protrusions with 850 nm OCT and micro-profilometry

Assessment of the spatial distribution of the protrusion-like structures provides a different approach to quantifying change. Applying a threshold to the three-dimensional micro-profilometry surface map in z-direction makes it possible to determine the fraction of the surface area that is covered by protrusion-like structures. The same approach can be applied to the 850 nm OCT surface data acquired from the iron oxide model system. Four steps, described in detail in S2.9 in the SI, were necessary to calculate this area fraction. Here, we evaluate a 40 μm and 70 μm threshold (Fig. 14). Evidently, the absolute fraction of the surface above the threshold is affected by changing the threshold value. Nevertheless, it seems that the absolute fractions calculated for the two types of data sets (OCT and micro-profilometry) are comparable. The trend based on the 850 nm OCT data indicates a slight increase in surface area that stabilised after T8. The trend based on the micro-profilometry shows no reliably recorded change, also due to the absence of the final time point. Overall, both trends indicate relatively little change in the surface area during the monitoring experiment.

Multispectral colorimetry coupled to micro-profilometry to monitor local colour changes

The final technique discussed is micro-profilometry combined with multispectral imaging, which allowed the calculation of local colorimetric

coordinates. Each measurement in the multispectral image corresponded to $250 \times 250 \mu\text{m}^2$ (1 pixel). The colorimetric coordinates were averaged over at least 3 points. By registering the multispectral images to the micro-profilometry surface maps, it became possible to calculate local ΔE values (CIE 1976) at a much higher spatial resolution than the commercially available colorimetry system (submillimetre versus 5 mm). Figure 15 shows this analysis for the iron oxide model system only, as the micro-profilometry data of the smalt systems had a low signal-to-noise ratio due to the absorption of the laser. The ΔE of the entire sample surface of the iron oxide model system (averaged from a $30 \times 30 \text{ mm}^2$ area) is in the range of 2–4, similar to the results obtained with the commercial system. In addition, two types of areas were characterised based on the micro-profilometry height map. Areas A, B and C correspond to flat areas that were unaffected by protrusion growth and areas 1, 2, 3, 4 and 5 correspond to “unstable” protrusions that increased in dimensions after T1 (Fig. 15a). From these two types of areas $L^*a^*b^*$ coordinates and ΔE were extracted and compared to the coordinates of the entire sample surface (Fig. 15c–e). The $L^*a^*b^*$ coordinates can be found in S2.8 of the SI. The ΔE values in the flat areas remain relatively constant (ΔE about 3). Interestingly, the ΔE values for the regions associated with unstable protrusions are higher ($\Delta E > 5$) than those for the flat areas, owing to an increase of L^* , a decrease of a^* and an oscillation of b^* values. An increase of L^* and a reduction of a^* could be a sign of thinning and/or disruption of the paint layer due to the pressure caused by the lead soaps. This phenomenon is indeed visible in photographs

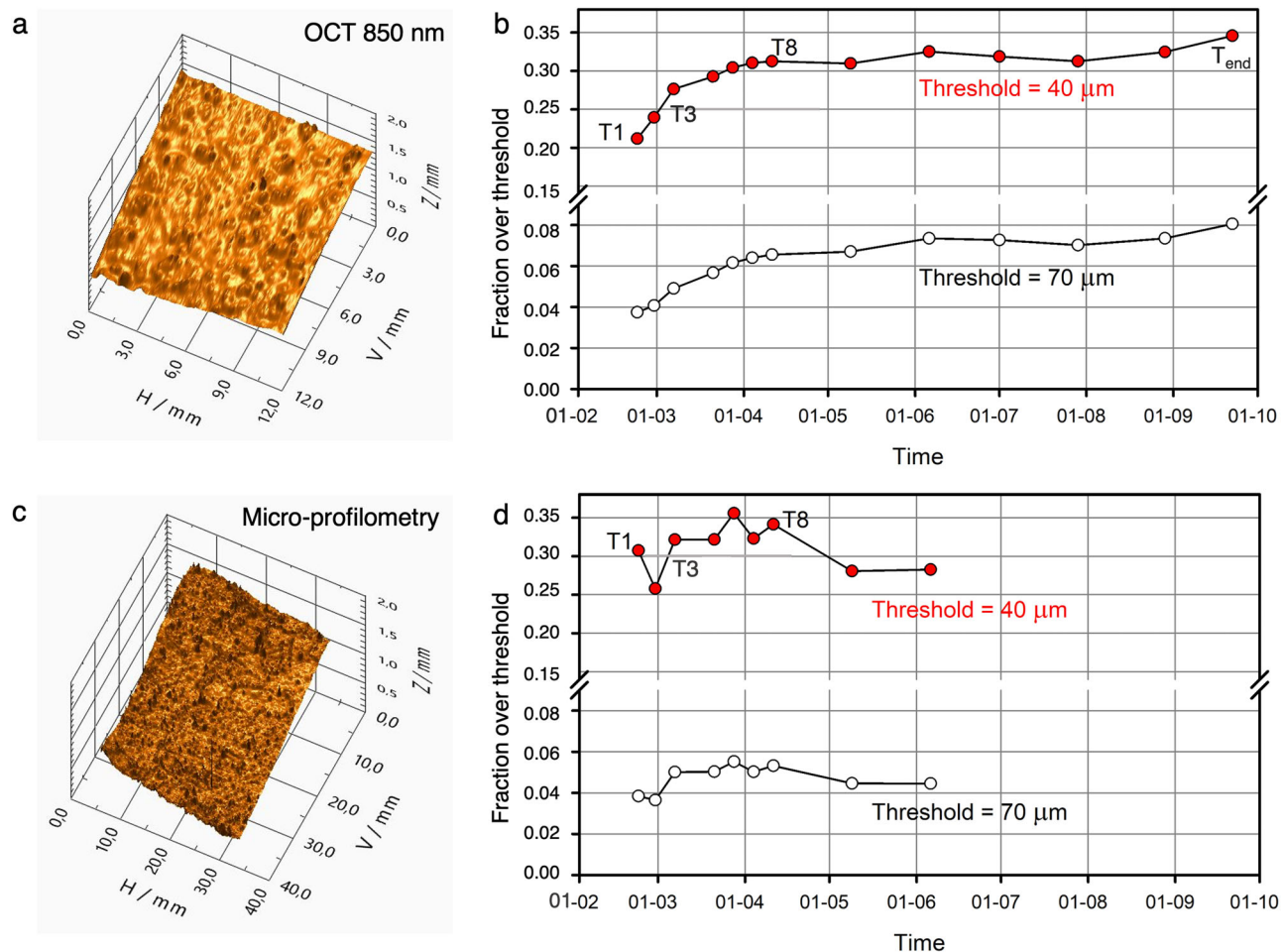


Fig. 14 | Comparison of the 850 nm OCT and micro-profilometry surface maps of the iron oxide model system. a, c The surface maps as recorded before correction. Note that the z-axis is stretched for better readability. **b, d** The growth of the

protrusions is evaluated by looking at the fraction of the surface above a certain threshold over time. Two thresholds (40 and 70 μm) are compared.

of the iron oxide sample and in cross-sections (see Table S1 in S1.3 of the SI), where the pale-yellow colour of the protrusion-like structures is visible through the thin iron oxide paint layer. Therefore, Fig. 15e indeed shows the change that is associated with protrusion growth.

Discussion

In this pilot study, we explored several technological approaches to non- or minimally invasively detect changes in lead soap protrusions in dynamic model systems with the aim of performing long-term monitoring of metal soap protrusions in paintings in the future. The model systems were created to form lead soaps in situ in a short time frame. To meet this condition, reactive components were added in substantial amounts that are not representative of the conditions in historical paintings. Cross-section analysis (microscopy and micro-chemical imaging) performed parallel to the monitoring experiment showed variation in the morphology of the active layer. In some areas, the active layer had expanded homogeneously, whereas in other areas, protrusion-like structures formed. Lead soap domains formed with sizes varying from several micrometres up to 100 μm in diameter. Interestingly, protrusion-like expansions that contained lead soaps in very small concentrations were observed, as detected by $\mu\text{-ATR-FTIR}$ imaging on cross-sections. It is unclear which mechanisms are responsible for the expansion of the active layer in those cases. These low concentrations of lead soaps in protrusion-like structures are reminiscent of model systems created by Romano et al. that formed zinc soap protrusions after four years that contained oily, gel-like inclusions⁴⁴. Despite their heterogeneity and

complex dynamics, the model systems were valuable tools for exploring monitoring approaches. They represented some of the complexities of long-term monitoring of real works of art, for example how reference points may alter over time and how the chemical processes responsible for the detected changes are not well understood. The cross-section analyses confirm that the model systems are dynamic systems, i.e. components in the active layer react, expand and move through the paint stratigraphy. Overall, it proved challenging to capture this change using the non- or minimally invasive monitoring approaches.

Portable external reflection FTIR did not detect characteristic vibration bands related to lead carboxylates due to low concentrations of lead soaps in the measured volume. While these low concentrations of lead soaps may be a feature specific to the model systems, it does illustrate an important limitation of the portable external FTIR for the early detection of metal soaps. Out of the three techniques that could be considered relatively accessible, X-radiography was successful in detecting and quantifying small changes related to lead soap protrusions. An important requirement is good contrast in absorption between the protrusion and the surrounding materials, which may be reduced where paint passages in historical paintings use pigments containing heavy elements. Raking light photography and colourimetry did detect change, but this change could not be explicitly related to the lead soap protrusions. The results of the raking light photography in combination with simple image analysis using a greyscale threshold, were strongly impacted by interfering factors, such as the canvas structure visible through the paint layer. Similarly, the colour change detected by the commercial

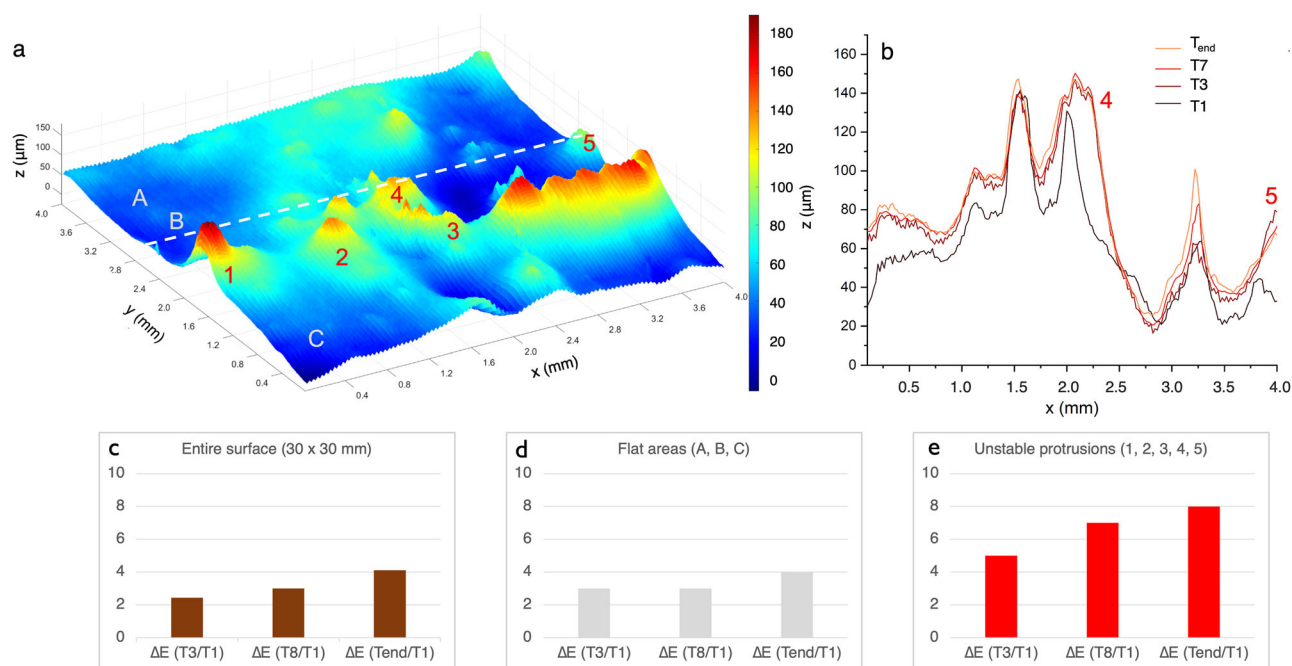


Fig. 15 | Multispectral colorimetry results coupled to micro-profilometry for iron oxide model system. a Micro-profilometry height map with flat areas A, B and C and unstable areas 1–5 indicated. **b** Line profiles corresponding to the white dashed line

in (a). Protrusions 4 and 5 are indicated. **c** Average ΔE values (CIE 1976) are calculated for the entire surface area of the sample. **d** Average ΔE values for flat areas **e** Average ΔE values for unstable protrusions.

colorimetry was overwhelmed by yellowing of the oil rather than lead soap protrusion growth.

When colorimetry with a much higher resolution was used and in combination with three-dimensional information from the micro-profilometry, a colour change that was specific to the protrusions could be isolated. In the case of all techniques providing three-dimensional surface and sub-surface information, resolution was critical for change quantification. Acoustic microscopy was used for the first time to detect and localise protrusions in this experiment, however the depth resolution was insufficient to quantify changes in the protrusion-like structures. Examination with the 850 nm OCT instrument revealed the importance of the measurement protocol adopted. The one used here, although usually sufficient for structural examination of paintings on canvas, was insufficient for correct estimation of protrusions size due to the large scan distance (80 μm in y -direction). However, this could be easily adjusted in subsequent studies. For the 1300 nm OCT instrument, which had sufficient depth of penetration and resolution ($20 \times 20 \times 3.48 \mu\text{m}^3$), the size of individual protrusions can be reliably measured over time. Micro-profilometry also provided sufficient resolution for the purpose of quantifying change in individual protrusions in paints where the composition allowed sufficient signal-to-noise ratio. However, for all 3D imaging techniques, even with sufficient resolution, baseline and angular tilt correction had to be considered in order to reliably follow individual protrusions over time.

As an alternative to monitoring individual protrusions, we quantified protrusion growth by evaluating the increase in height of the total model system surface compared to a threshold. The 850 nm OCT surface data indicated that the surface area occupied by protrusion-like structures increased, but the micro-profilometry data showed no signs of increase. Overall, the non- or minimally invasive monitoring experiment yielded only very small changes in the protrusions in the model systems.

The pilot study generated several learning points that help answer the question, “How to approach long-term monitoring of chemical dynamics in oil paintings?” It became clear that a hypothesis on the expected change is necessary for developing long-term monitoring protocol, especially quantitatively. It is very challenging to measure change without knowing beforehand which change is expected. This challenge sets long-term

monitoring apart from detection and localisation. Condition phenomena in paintings can have multiple properties that can be individually monitored. It should be clear from the outset how a change in these properties relates to the research question. This is important because the degree of change that one detects depends strongly on how that change is defined. For example, in the micro-profilometry data of this pilot study, change in individual protrusions was evaluated in terms of growth in the z -direction. Therefore, other changes in protrusion shape due to aggregation or merging of the lead-containing compounds were overlooked.

Conclusion

This pilot study found that three-dimensional (sub-) surface scanning techniques are suitable for monitoring lead soap protrusions in oil paintings if they provide sufficient lateral and depth resolution. It was possible to detect small-scale changes in the size and shape of protrusion-like structures in painted multi-layered model systems, although no specific chemical identification of lead soaps is obtained. Critical for quantifying small changes is the alignment of the 3D profiles acquired over different points of time. For alignment or registration, reference points that do not change over time should be selected. As long-term monitoring will likely focus on regions of interest in a painting that is unstable, care must be taken to select robust reference points. In addition, X-radiography proved suitable for detecting changes in the spatial distribution of metal soap protrusions. By systematically approaching X-radiograph acquisitions that are already routinely carried out in many museums, this could form a relatively accessible tool for long-term monitoring of protrusions in easel paintings.

In conclusion, long-term monitoring of chemical dynamic processes in paintings is challenging for a variety of reasons. This pilot study helps to develop and refine a hypothesis about the expected changes around lead soap protrusions and improving measurement protocols. Despite the challenges that long-term monitoring poses, it has the potential to generate valuable insights into material degradation and the environmental response to support the preservation of oil-based paintings.

Data availability

No datasets were generated or analysed during the current study.

Received: 28 May 2024; Accepted: 19 December 2024;

Published online: 22 February 2025

References

- Cather, S. In *Conserving the Painted Past: Developing Approaches to Wall Painting Conservation* (eds Gowing, R. & Heritage, A.) 64–74 (Routledge, 2003).
- Wong, L., Lardinois, S., Hussein, H., Salem Bedair, R. M. & Agnew, N. Ensuring the sustainability of conservation: monitoring and maintenance in the tomb of Tutankhamen. In: *Preprints of the ICOM Committee for Conservation 19th Triennial Meeting, Beijing 17–21 May 2021* (ed. Bridgland, J.) Art. 232 (International Council of Museums, 2021).
- Hill, J. A. & Haeusler, I. L. Intervention vigilance in conservation: Lessons from the medical profession. In: *Preprints of the ICOM Committee for Conservation 19th Triennial Meeting, Beijing 17–21 May 2021* (ed. Bridgland, J.) Art. 91 (International Council of Museums, 2021).
- Group BIZOT. The BIZOT Green Protocol. 2023. <https://www.cimam.org/sustainability-and-ecology-museum-practice/bizot-green-protocol/> (Accessed 23 Apr 2023).
- Fontana, R. et al. Application of non-invasive optical monitoring methodologies to follow and record painting cleaning processes. *Appl. Phys. A*. **121**, 957–966 (2015).
- Iwanicka, M. et al. Complementary use of optical coherence tomography (OCT) and reflection FTIR spectroscopy for in-situ non-invasive monitoring of varnish removal from easel paintings. *Microchem. J.* **138**, 7–18 (2018).
- Iwanicka, M. et al. Congregation leaving the Reformed Church in Nuenen by Vincent van Gogh: a combined multi-instrumental approach to analyse the painting's stratigraphy in support of varnish removal. *Herit. Sci.* **10**, 1–15 (2022).
- Liang, H. et al. Optical coherence tomography in archaeological and conservation science—a new emerging field. In: *Proc. 1st Canterbury Workshop on Optical Coherence Tomography and Adaptive Optics* (ed. Podoleanu, A.) (SPIE, 2008).
- Barazzetti, L. et al. Monitoring the cathedral of Milan: an archive with more than 50 years of measurements. In: *Computational Science and Its Applications—ICCSA 2022* 575–590 (Springer, 2022).
- Zehnder, K. Long-term monitoring of wall paintings affected by soluble salts. *Environ. Geol.* **52**, 353–367 (2007).
- Ormsby, B., Lundsbaekken, O. E., Monico, L., Bartoletti, A. & Lee, J. Revisiting cleaned acrylic emulsion painting surfaces ten years on: Observations and reflections. In: *Preprints of the ICOM Committee for Conservation 19th Triennial Meeting, Beijing 17–21 May 2021* (ed. Bridgland, J.) Art. 93 (International Council of Museums, 2021).
- Giozzo, E. & Ionescu, C. Pigments—Lead-based whites, reds, yellows and oranges and their alteration phases. *Archaeol. Anthropol. Sci.* **14**, 17 (2022).
- Janssens, K. et al. In *Analytical Chemistry for Cultural Heritage* (ed. Mazzeo, R.) 77–128 (Springer, 2017).
- Miliani, C. et al. Photochemistry of artists' dyes and pigments: towards better understanding and prevention of colour change in works of art. *Angew. Chem. Int. Ed.* **57**, 7324–7334 (2018).
- Bronken, I. A. T. & Boon, J. J. In *Issues in Contemporary Oil Paint* (ed. van den Berg, K. J.) 247–262 (Springer, 2014).
- Helwig, K. et al., editors. *Conservation of Modern Oil Paintings* (Springer, 2020).
- Hermans, J. J., Keune, K., Van Loon, A. & Iedema, P. D. *Metal Soaps in Art* (eds Casadio, F. et al.) 47–67 (Springer, 2019).
- Russo, S., Brambilla, L., Thomas, J. B. & Joseph, E. But aren't all soaps metal soaps? A review of applications, physico-chemical properties of metal soaps and their occurrence in cultural heritage studies. *Herit. Sci.* **11**, 172 (2023).
- Robinet, L. & Corbeil, M. C. The characterization of metal soaps. *Stud. Conserv.* **48**, 23–40 (2003).
- van den Berg, K. J. & Burnstock, A. *Metal Soaps in Art* (eds Casadio, F. et al.) 329–342 (Springer, 2019).
- Burnstock, A. In *Metal Soaps in Art* (eds Casadio, F. et al.) 243–262 (Springer, 2019).
- Noble, P. In *Metal Soaps in Art* (eds Casadio, F. et al.) 1–22 (Springer, 2019).
- Centeno, S. A. & Mahon, D. The chemistry of aging in oil paintings: metal soaps and visual changes. *Metrop. Mus. Art. Bull.* **67**, 12–19 (2009).
- Boon, J. J., van der Weerd, J., Keune, K., Noble, P. & Wadum J. Mechanical and chemical changes in Old Master paintings: dissolution, metal soap formation and remineralization processes in lead pigmented ground/intermediate paint layers of 17th century paintings. In: *Preprints of the ICOM Committee for Conservation 13th Triennial Meeting, Rio de Janeiro 21–28 Sept 2002* (ed. Antomarchi, C.) 401–406 (James and James, 2002).
- Salvant, J. et al. In *Metal Soaps in Art* (eds Casadio, F. et al.) 375–391 (Springer, 2019).
- Cotte, M. et al. Lead soaps in paintings: friends or foes? *Stud. Conserv.* **62**, 2–23 (2017).
- van Loon, A. et al. Investigation of the dynamic processes underlying lead soap-related degradation phenomena in multi-layer model systems. [Poster]. In: *Metal Soaps in Art Conference, Amsterdam 14–15 March 2016* (2016).
- Sawicka, A. Clearing the 'Haze' of Inorganic Efflorescence [Master's Thesis]. Courtauld Institute of Art (2013).
- IPERION HS. MOLAB. 2019. Available from: <https://www.iperionhs.eu/molab/> (Accessed 30 Apr 2024).
- Gabrieli, F. et al. Revealing the nature and distribution of metal carboxylates in Jackson Pollock's *Alchemy* (1947) by micro-attenuated total reflection FT-IR spectroscopic imaging. *Anal. Chem.* **89**, 1283–1289 (2017).
- Garrappa, S. et al. Non-invasive identification of lead soaps in painted miniatures. *Anal. Bioanal. Chem.* **413**, 263–278 (2021).
- Izzo, F. C., Kratter, M., Nevin, A. & Zendri, E. A critical review on the analysis of metal soaps in oil paintings. *ChemistryOpen* **10**, 904–921 (2021).
- Rosi, F. et al. In *Metal Soaps in Art* (eds Casadio, F. et al.) (Springer, 2019).
- Vichi, A. et al. An exploratory study for the noninvasive detection of metal soaps in paintings through optical coherence tomography. In: *Proceedings of Optics for Arts, Architecture, and Archaeology VII Conference, Munich 24–26 June 2019*. (eds Liang, H., Groves, R. & Targowski, P.) 14–22 (SPIE, 2019).
- van den Berg, K. et al. In *Van Gogh's Sunflowers Illuminated Art Meets Science* (eds Hendriks, E. et al.) (Amsterdam University Press/Van Gogh Museum Amsterdam, 2019).
- Broers, F. T. et al. Correlated x-ray fluorescence and ptychographic nano-tomography on Rembrandt's *The Night Watch* reveals unknown lead "layer". *Sci. Adv.* **9**, ead9394 (2023).
- Striova, J. et al. Spectral imaging and archival data in analysing Madonna of the Rabbit paintings by Manet and Titian. *Angew. Chem.* **130**, 7530–7534 (2018).
- Carcagni, P. et al. Spectral and colorimetric characterisation of painted surfaces: A Scanning device for the imaging analysis of paintings. In: *Proceedings of Optical Methods for Arts and Archaeology Conference, Munich 13–17 June 2005* 235–244 (SPIE, 2005).
- Ferreira, T. & Rasband, W. *ImageJ User Guide* 1.46. (National Institutes of Health, 2012).
- Targowski, P., Kowalska, M., Sylwestrzak, M. & Iwanicka, M. *Optical Coherence Tomography and Its Non-Medical Applications* (ed. Wang, M.) 147–164 (IntechOpen, 2020).

41. Fontana, R. et al. High-resolution 3D survey of artworks. In: *Proceedings of Optical Metrology in Production Engineering Conference, Strasbourg 27–30 April 2004* (eds Osten, W. & Takeda, M.) 719–726 (SPIE, 2004).
42. Karagiannis, G., Alexiadis, D. S., Damtsios, A., Sergiadis, G. D. & Salpistis, C. Three-dimensional nondestructive “sampling” of art objects using acoustic microscopy and time–frequency analysis. *IEEE Trans. Instrum. Meas.* **60**, 3082–3109 (2011).
43. Liang, H., Lange, R., Peric, B. & Spring, M. Optimum spectral window for imaging of art with optical coherence tomography. *Appl Phys. B.* **111**, 589–602 (2013).
44. Romano, C. et al. Characterization of zinc carboxylates in an oil paint test panel. *Stud. Conserv.* **65**, 14–27 (2020).
45. Cotte, M. et al. Watching kinetic studies as chemical maps using open-source software. *Anal. Chem.* **88**, 6154–6160 (2016).

Acknowledgements

JRD would like to thank Jolanda van Iperen for technical support and Francesca Gabrieli and Momoko Okuyama for useful discussions. This research was conducted within IPERION HS Task 5.1 Project 2 funded by the European Union, H2020-INFRAIA-2019-1 under GA 871034.

Author contributions

J.R.D.: conceptualisation; methodology; investigation; and writing – original draft. P.T., M.S., M.I., J.S., D.Q.B., A.C., R.F., F.R., F.S., L.C., B.D., L.M., M.L., P.A., C.S.C., H.L., J.A.H., D.M., G.K., S.A.: methodology; investigation; writing – review. J.J.H.: writing – review. K.K.: conceptualisation; methodology; supervision; writing – review.

Competing interests

The authors declare no competing interests.

Additional information

Supplementary information The online version contains supplementary material available at <https://doi.org/10.1038/s40494-025-01583-4>.

Correspondence and requests for materials should be addressed to Jorien R. Duivenvoorden.

Reprints and permissions information is available at <http://www.nature.com/reprints>

Publisher’s note Springer Nature remains neutral with regard to jurisdictional claims in published maps and institutional affiliations.

Open Access This article is licensed under a Creative Commons Attribution-NonCommercial-NoDerivatives 4.0 International License, which permits any non-commercial use, sharing, distribution and reproduction in any medium or format, as long as you give appropriate credit to the original author(s) and the source, provide a link to the Creative Commons licence, and indicate if you modified the licensed material. You do not have permission under this licence to share adapted material derived from this article or parts of it. The images or other third party material in this article are included in the article’s Creative Commons licence, unless indicated otherwise in a credit line to the material. If material is not included in the article’s Creative Commons licence and your intended use is not permitted by statutory regulation or exceeds the permitted use, you will need to obtain permission directly from the copyright holder. To view a copy of this licence, visit <http://creativecommons.org/licenses/by-nc-nd/4.0/>.

© The Author(s) 2025